Plasma Sources Science and Technology

PAPER

Noninvasive THz-TDS measurements of plasma bounded and optically shielded by Hall thruster wall material

To cite this article: Nathan P Brown *et al* 2021 *Plasma Sources Sci. Technol.* **30** 075027

IOP Publishing | Plasma Sources Science and Technology

Plasma Sources Sci. Technol. **30** (2021) 075027 (11pp) https://doi.org/10.1088/1361-6595/ac12be

Noninvasive THz-TDS measurements of plasma bounded and optically shielded by Hall thruster wall material

Nathan P Brown[1,2,*], Muhannad M Eladl[1], Adam M Steinberg[1], Jason A Deibel[3] and Mitchell L R Walker[1]

[1] School of Aerospace Engineering, Georgia Institute of Technology, Atlanta, Georgia, United States of America
[2] Pulsed Power Sciences, Sandia National Laboratories, Albuquerque, New Mexico, United States of America
[3] Department of Physics, Wright State University, Dayton, Ohio, United States of America

E-mail: npbrown@sandia.gov

Received 21 May 2021
Accepted for publication 8 July 2021
Published 29 July 2021

Abstract

We experimentally demonstrate the capability of terahertz time-domain spectroscopy (THz-TDS) to noninvasively measure the electron density and collision frequency of plasma bounded and optically shielded by Hall thruster wall material. This paper augments the standard THz-TDS plasma diagnostic theory to account for plasma boundaries, presents THz optical property measurements of three different wall materials (grades M, M26, and HP boron nitride composite), and provides electron density and collision frequency measurements of an inductively coupled plasma bounded and optically shielded by each wall material. We find that the electron density measurement capability is weakly impacted by the boundaries, whereas the electron collision frequency measurement capability is strongly reduced by the boundaries. The bounded plasma electron density trends deviate substantially from those of the unbounded plasma.

Keywords: Hall thruster, boron nitride, plasma diagnostics, terahertz, terahertz time-domain spectroscopy

(Some figures may appear in colour only in the online journal)

1. Introduction

The Hall thruster is a spacecraft propulsion device that electrostatically accelerates plasma ions to generate thrust. Its capability to provide moderate specific impulse (1000–3000 s) and thrust (0.1–1 N) has made it a mainstay propulsion technology [1–4]. Since the 1971 launch of the Russian METEOR-18, Hall thrusters have flown on hundreds of commercial and government spacecraft [5].

Shown schematically in figure 1, the Hall thruster is an annular $E \times B$ plasma discharge that ionizes neutral propellent via collisions with electrons thermionically emitted from a hollow cathode. The electric field, established between the cathode and anode, points along the thruster axis, and the magnetic field, established by solenoids arranged around the annulus, points along the thruster radius. The crossed electric and magnetic fields trap the ionizing electrons in an azimuthal Hall drift, thereby enhancing ionization efficiency and enabling maintenance of the discharge plasma. Ions, due to their comparatively larger mass, have a gyroradius larger than the discharge channel and are consequently not trapped in the Hall drift. Ions respond primarily to the axial electric field and are accelerated into the thruster exhaust.

The Hall thruster wall structure that forms the discharge annulus confines the plasma and shields the solenoids from ion bombardment. The walls are typically comprised of boron

* Author to whom any correspondence should be addressed.

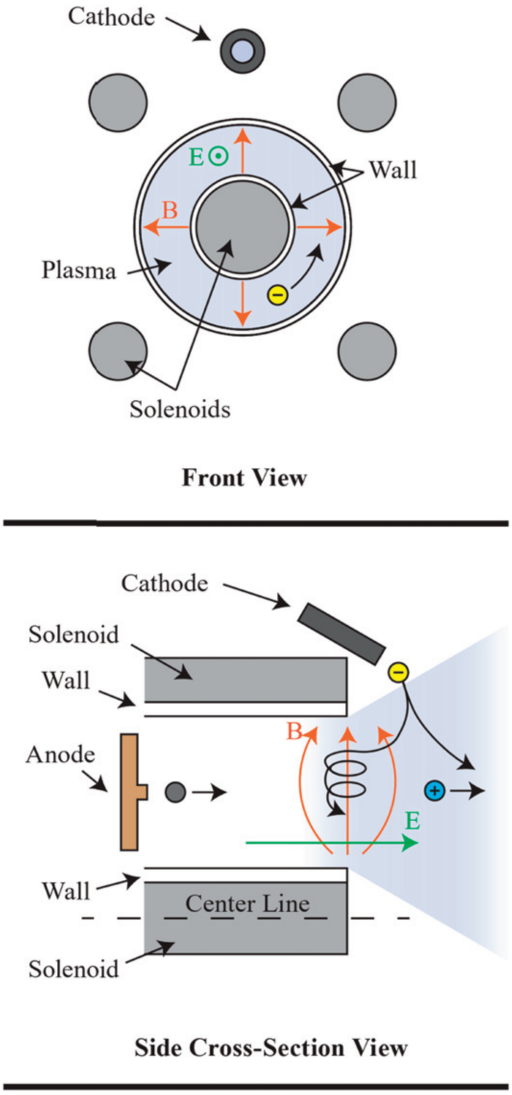

Figure 1. Hall thruster schematic.

nitride (BN) or BN-silica (BN-SiO_2) composite, materials selected for their low sputtering yield, low electrical conductivity, and favorable secondary electron emission rate. Gradual erosion of the walls by plasma sputtering eventually exposes the solenoids to plasma ions, effectively ending thruster life [6].

Despite more than five decades of thruster development and study, the plasma physics driving Hall thruster operation is still not completely understood. The anomalous transport of electrons across magnetic field lines and the growth of anomalous erosion ridges on discharge walls, for example, have thus far eluded explanation and self-consistent first-principles modeling [6–9]. The inability to model these phenomena limits the community's capability to improve thruster efficiency and lifetime.

Open plasma physics questions remain, in part, due to the lack of diagnostic capability inside the region between the Hall thruster walls. This so-called Hall thruster channel has been previously investigated with electrostatic probes, but physical probes are inherently invasive [7, 10–12]. Their presence interferes with thruster operation and casts measurement reliability into doubt. Noninvasive optical diagnostics are now routinely employed by the Hall thruster community for plume measurements, but contemporary techniques are not well-suited for channel diagnostics. Stalwart optical diagnostics, such as optical emission spectroscopy [13], laser-induced fluorescence [14], and laser Thomson scattering [15], require the emission and/or detection of radiation with wavelengths that do not transmit through Hall thruster wall material.

A relatively novel plasma diagnostic technique with the potential to perform Hall thruster channel measurements is terahertz time-domain spectroscopy (THz-TDS) [16–23]. THz-TDS probes plasma with broadband pulsed THz radiation to measure line-integrated electron density and collision frequency. Previous work has demonstrated the capability of THz-TDS to achieve mm-scale spatial resolution [17] and ps-scale temporal resolution [16, 23]. Pulsed THz radiation has also been shown to transmit through various grades of BN and BN-SiO_2 composite, and the pulsed nature of the radiation can enable measurements in bounded plasma without interference from Fabry–Pérot (FP) reflections [24–26].

In a previous study [19], we experimentally demonstrated the capability of THz-TDS to make electron density and collision frequency measurements in plasma optically shielded (but not bounded) by a relevant BN-SiO_2 composite. Placing BN-SiO_2 in the THz pulse path such that the THz radiation had to propagate through the BN-SiO_2 before reaching the plasma did not significantly change the measurement results. Comparing measurements made with and without BN-SiO_2 in the pulse path, the maximum observed difference in measured electron density was less than 7% and the maximum difference in electron collision frequency was less than 10%. In that work, the raw data were analyzed with a conventional method [27]. Analyzing the raw data with a recently developed Bayesian framework [28] that corrects for common THz-TDS measurement artifacts reduces maximum differences in electron density and collision frequency to 5% and 9%, respectively, and reveals that these differences are within the uncertainty of the measurement.

In this paper, we extend our previous efforts by performing measurements of an inductively coupled plasma (ICP) discharge that is both optically shielded and bounded by Hall thruster wall material. Though motivated by an interest in expanding Hall thruster diagnostic capabilities, our measurements additionally enable us to investigate a plasma that, due to the boundaries, is neither accessible to standard physical probe diagnostics nor easily modeled. Our results indicate the plasma boundaries significantly impact the discharge physics and, though not directly applicable to Hall thruster discharge physics, highlight the importance of noninvasive diagnostics for bounded plasmas.

This paper is organized as follows: section 2 provides the standard THz-TDS plasma equations and derives the relations required for bounded plasma measurements; section 3 describes the experimental setup; and section 4 presents and discusses the measurement results.

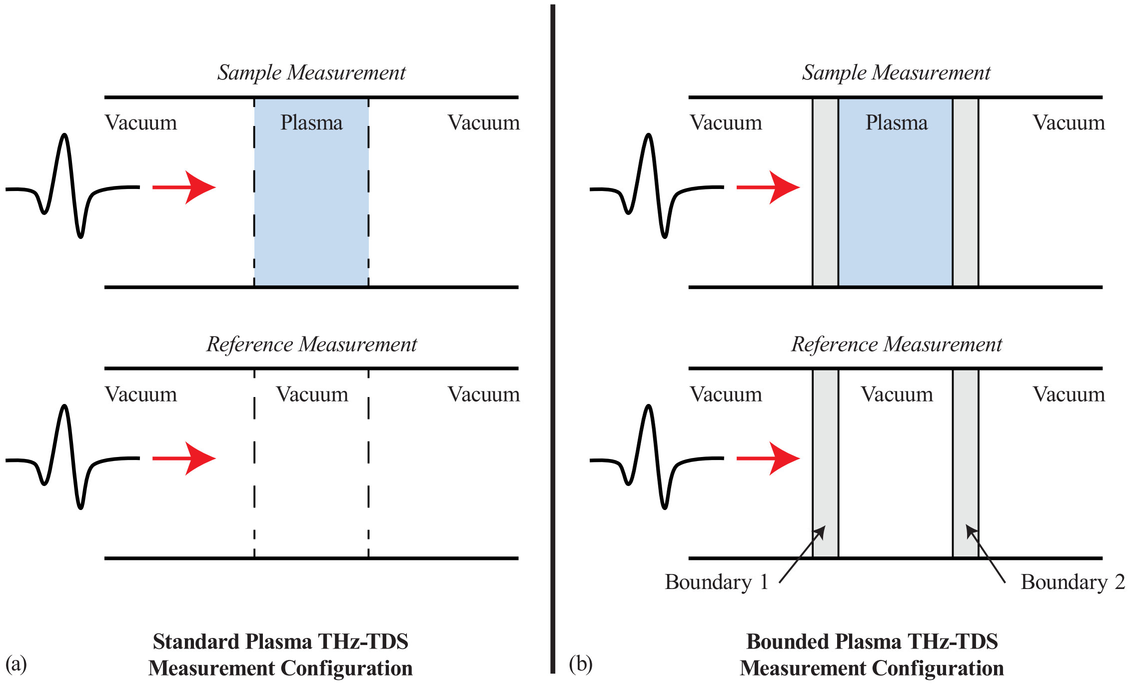

Figure 2. Sample and reference THz-TDS measurement schematics for (a) standard and (b) bounded configurations.

2. THz-TDS equations

This section provides an overview of the THz-TDS equations. Section 2.1 gives the standard equations used to determine the electron density and collision frequency from THz-TDS measurements. Section 2.2 augments the standard equations to incorporate boundary effects.

2.1. Standard equations

The extraction of plasma properties from THz-TDS data requires the comparison of sample and reference electric fields. As shown in figure 2(a), the sample field (E_s) is recorded with plasma in the THz pulse path, and the reference field (E_r) is recorded without plasma in the THz pulse path.

Assuming the plasma is not bounded along the THz pulse path, scattering of pulse energy out of the path is negligible, and the (real) refractive index mismatch at the plasma–vacuum interface is sufficiently small that pulse reflections can be ignored, the sample and reference electric field spectra ($\widehat{E}_s$ and $\widehat{E}_r$) are related to the complex plasma refractive index ($\tilde{n}_p$) by

$$\frac{\widehat{E}_s(\omega)}{\widehat{E}_r(\omega)} = \exp\left[i\frac{\omega}{c}\int_0^L \{\tilde{n}_p(\omega, z) - 1\}\,dz\right], \tag{1}$$

where ω is the angular frequency component of the probing THz radiation, c is the vacuum speed of light, L is the plasma length, and z is the distance along the axis of pulse propagation [25, 29, 30]. If the plasma is uniform along the z direction, equation (1) further simplifies to

$$\frac{\widehat{E}_s(\omega)}{\widehat{E}_r(\omega)} = \exp\left[i\frac{\omega L}{c}\{\tilde{n}_p(\omega) - 1\}\right]. \tag{2}$$

In many cases, equation (2) is also a valid expression for the average plasma refractive index in non-uniform plasmas. The error incurred for ignoring the distribution is typically negligible, as long as the radiation frequency components used to compute the average properties are not near plasma cut-off [31].

The complex plasma refractive index, in turn, is related to the angular plasma frequency (ω_p) and angular electron collision frequency (ν) by

$$\tilde{n}_p^2(\omega) = 1 - \frac{\omega_p^2}{\omega(\omega + i\nu)}. \tag{3}$$

The plasma frequency is a function of the electron density (n_e), elementary charge (e), permittivity of free space (ε_0), and electron mass (m_e):

$$\omega_p^2 = \frac{n_e e^2}{\varepsilon_0 m_e}. \tag{4}$$

The refractive index is strictly valid for a Lorentz plasma, in which magnetic field and electron temperature effects may be neglected [32, 33]. Most electric propulsion plasma environments, including that of the Hall thruster discharge, meet these requirements [31].

2.2. Bounded plasma equations

Plasma boundaries cause THz pulse reflection effects that must be accounted for in the THz-TDS equations. Figure 2(b) shows the sample and reference measurement configurations with boundaries in the pulse path.

Applying the general derivation method of Duvillaret *et al* [25] to the bounded plasma measurement configuration, the ratio of the reference and sample electric field spectra becomes

$$\frac{\widehat{E}_{\mathrm{s}}(\omega)}{\widehat{E}_{\mathrm{r}}(\omega)} = D(\omega)\,\mathrm{FP}(\omega)\exp\left[i\frac{\omega L}{c}\left\{\tilde{n}_{\mathrm{p}}(\omega) - 1\right\}\right], \quad (5)$$

where

$$D(\omega) = \frac{D_{\mathrm{b_1 p}}(\omega)\,D_{\mathrm{pb_2}}(\omega)}{D_{\mathrm{b_1 v}}(\omega)\,D_{\mathrm{vb_2}}(\omega)} \quad (6)$$

and $D_{\mathrm{b_1 p}}$, $D_{\mathrm{pb_2}}$, $D_{\mathrm{b_1 v}}$, and $D_{\mathrm{vb_2}}$ are the transmission coefficients from boundary 1 to plasma, plasma to boundary 2, boundary 1 to vacuum, and vacuum to boundary 2, respectively, and FP quantifies the impact of FP reflections within the bounded region. The transmission coefficients are functions of the complex boundary, plasma, and vacuum refractive indices, according to:

$$D_{ab}(\omega) = \frac{2\tilde{n}_a(\omega)}{\tilde{n}_a(\omega) + \tilde{n}_b(\omega)}. \quad (7)$$

FP reflections may be ignored if the first FP-reflected pulse arrives in the incident pulse at a time greater than the measured pulse duration. The arrival time (t) of the first FP-reflected pulse in the sample measurement is given by

$$t = \frac{2n_{\mathrm{p}}(\omega)\,L}{c}, \quad (8)$$

where n_{p} is the real component of the complex plasma refractive index [26]. The real plasma refractive index is typically near unity, and most salient THz pulse information is contained within a few picoseconds. Therefore, FP reflections may be ignored in measurements of plasmas with mm-scale and longer length via the application of appropriate temporal windowing in analysis of the incident pulse. This capability to ignore FP reflections greatly simplifies the analysis and is enabled by the pulsed nature of the probing THz radiation. FP reflections cannot be ignored in the analysis of measurements made with continuous-wave diagnostics, such as microwave interferometry.

Setting the FP term to unity and substituting equations (6) and (7) into equation (5) yields:

$$\frac{\widehat{E}_{\mathrm{s}}(\omega)}{\widehat{E}_{\mathrm{r}}(\omega)} = T(\omega)\exp\left[i\frac{\omega L}{c}\left\{\tilde{n}_{\mathrm{p}}(\omega) - 1\right\}\right], \quad (9)$$

where

$$T(\omega) = \frac{\tilde{n}_{\mathrm{p}}(\omega)\left[\tilde{n}_{\mathrm{b_1}}(\omega) + 1\right]\left[\tilde{n}_{\mathrm{b_2}}(\omega) + 1\right]}{\left[\tilde{n}_{\mathrm{b_1}}(\omega) + \tilde{n}_{\mathrm{p}}(\omega)\right]\left[\tilde{n}_{\mathrm{b_2}}(\omega) + \tilde{n}_{\mathrm{p}}(\omega)\right]}. \quad (10)$$

The complex refractive indices of boundary 1 and boundary 2 are $\tilde{n}_{\mathrm{b_1}}$ and $\tilde{n}_{\mathrm{b_2}}$, respectively. These must be measured independently to enable extraction of the plasma complex refractive index. The complex boundary refractive index ($\tilde{n}_{\mathrm{b}}$) is related to the real refractive index (n_{b}) and extinction coefficient (α_{b}) by

$$\tilde{n}_{\mathrm{b}}(\omega) = n_{\mathrm{b}}(\omega) + \frac{c}{\omega}\frac{i}{2}\alpha_{\mathrm{b}}(\omega). \quad (11)$$

In this work, equation (9) is solved for the electron density and collision frequency with input sample and reference electric field spectra via a Bayesian analysis framework described in detail elsewhere [28]. The framework corrects for delay line registration error and refraction of the THz beam away from the detector by modifying the phase and magnitude, respectively, of equation (9) to account for these measurement artifacts. The Bayesian framework additionally provides robust uncertainty quantification.

3. Experimental setup

This section discusses the experimental setup of the bounded plasma measurements. The THz-TDS system is described in section 3.1, the plasma discharge in section 3.2, and the plasma boundaries in section 3.3.

3.1. THz-TDS system

As shown in figure 3, the THz-TDS system operates in a pump–probe configuration: THz radiation is generated via optical pumping of a photoconductive antenna (PCA) and detected electro-optically via optical probing of a ⟨110⟩ zinc telluride (ZnTe) crystal [34, 35].

Ultrashort laser pulses (<50 fs) generated by a mode-locked Ti:Sapphire laser (Coherent Vitara-T HP) with 100 MHz repetition rate are focused onto the 5 μm PCA (BATOP PCA-60-05-10-800-h) dipole gap formed between gold electrodes patterned onto a low temperature-grown gallium arsenide substrate. The average laser pump power is limited to 5 mW to avoid damaging the PCA. The laser-induced photoelectrons respond to an externally applied voltage bias (15 VDC) to produce a transient current that radiates as a THz pulse. The THz pulse is coupled to air with a hyper-hemispherical high-resistivity float-zone silicon lens and collimated to a diameter of approximately 40 mm, steered into the plasma, and focused onto the ZnTe crystal by gold parabolic mirrors.

The ultrashort laser pulses in the probe beam copropagate through the ZnTe crystal (Eskma Optics ZnTe-1000H) with the THz pulses at identical polarization and orientation. The ZnTe crystal has a thickness of 1 mm and is oriented such that the THz and probe pulses propagate along the [110] axis with polarizations 45° from the [001] axis [36, 37]. Each THz pulse induces birefringence in the ZnTe crystal, thereby causing a differential phase retardation in each probing laser pulse that is linearly proportional to the electric field strength of the THz pulse. The differential phase retardation in the probe pulse is measured using a quarter-wave plate, Wollaston prism, and balanced photodetector connected to a lock-in amplifier (LIA) and computer running a custom LabVIEW virtual instrument.

An optical chopper placed in the probe beam provides a reference signal for the LIA. The fs-scale probe pulses are scanned across the ps-scale THz pulses with an optical delay line in the pump beam. The total scan time is approximately 5 min for each pulse. Group velocity dispersion is mitigated through the use of ultrafast optics designed for 800 nm and pre-compensated for with a pulse compressor (Coherent CPC II) upstream of the pump and probe beam split.

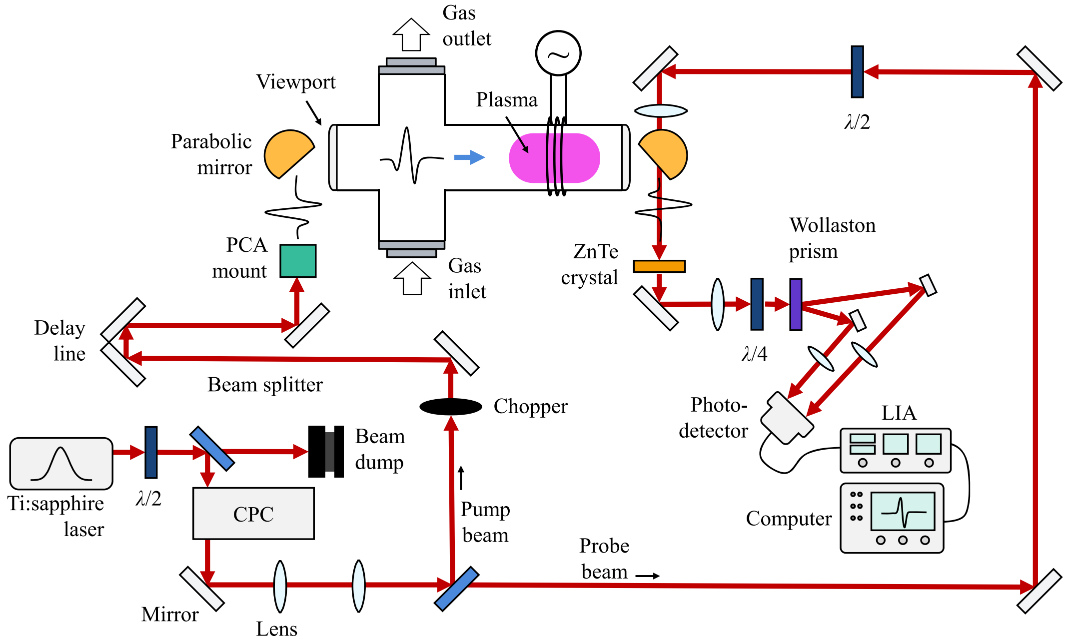

Figure 3. Schematic of THz-TDS system and plasma discharge (CPC: pulse compressor, LIA: lock-in amplifier, PCA: photoconductive antenna, $\lambda/2$: half-wave plate, $\lambda/4$: quarter-wave plate).

3.2. Plasma discharge

Figure 3 also shows a schematic of the radio frequency (RF) ICP discharge. The discharge chamber is a quartz tube cross (50 mm outer diameter, 3 mm wall thickness) inspired by the design of Ando *et al* [18]. The quartz is connected to KF vacuum flanges by quick-connect couplings (Kurt J. Lesker QF50XVC200). THz pulses enter and exit the vacuum chamber via viewports with Z-cut crystalline quartz windows (Torr Scientific BKVPZ50NQZ). The chamber is evacuated by a rotary-vane mechanical pump (Pfeiffer Adixen PASCAL 2021SD) to a base pressure of 1 mTorr, as measured by a convection pressure gauge (Kurt J. Lesker KJL275807LL) near the gas outlet. Ultra-high purity (99.999%) argon is fed into the discharge by a regulator and precision flow meter. Pressure values outputted by the pressure gauge are corrected for argon according to fits made from argon calibration data provided by the manufacturer.

RF power is coupled to the plasma via a three-turn hollow copper antenna wrapped around the glass tube. An unbalanced 13.56 MHz RF signal is generated by an RF power supply (Materials Science, Inc. RF-3-XIII), tuned by an RF radio antenna tuner (Palstar HF-AUTO), and converted to a balanced signal by a custom 1000 Ω current balun connected to each end of the antenna. Power is carried between devices by 50 Ω RG400 coaxial patch cables with UHF connectors (Pasternack PE3743 series). The plasma discharge is always operated with a standing wave ratio of 1.05 or less, and forward power drift was observed to remain within ±1 W throughout the duration of all THz-TDS measurements. An electrically grounded Faraday cage surrounding the antenna prevents stray electromagnetic radiation from interfering with THz-TDS measurements.

Across the operating conditions presented here, the discharge generates an unbounded uniform plasma length of approximately 12 cm. Bounded plasma measurements were therefore recorded with boundaries placed 10 cm apart to ensure plasma-boundary contact.

3.3. Plasma boundaries

Three different Hall thruster-relevant materials were used as boundaries in this study: grades M, M26, and HP BN composite manufactured by Saint-Gobain Ceramics. Each grade is formed by hot-pressing hexagonal close-packed (hcp) BN platelets in an amorphous binder material. According to the manufacturer, grade HP is >95% hcp BN and <5% calcium borate ($Ca_3B_2O_6$) binder by weight; grade M26 is 60% hcp BN and 40% SiO_2 by weight; and grade M is 40% hcp BN and 60% SiO_2 by weight.

Stock material provided by Saint-Gobain was machined into disks with 47 mm diameter so that the disks approximately filled the inner diameter of the ICP discharge. The disks were machined to a thickness of 0.3 in to be representative of the thickness of a standard Hall thruster wall. An additional set of disks with a thickness of 0.1 in was machined from the grade M26 stock material for additional measurements. The hot-press direction of each disk is parallel to the disk axis, so THz pulses propagated normal to the BN platelets (i.e. as ordinary rays).

4. Results and discussion

This section presents and discusses THz-TDS measurement results. Section 4.1 shows measured wall material optical properties, section 4.2 provides bounded plasma

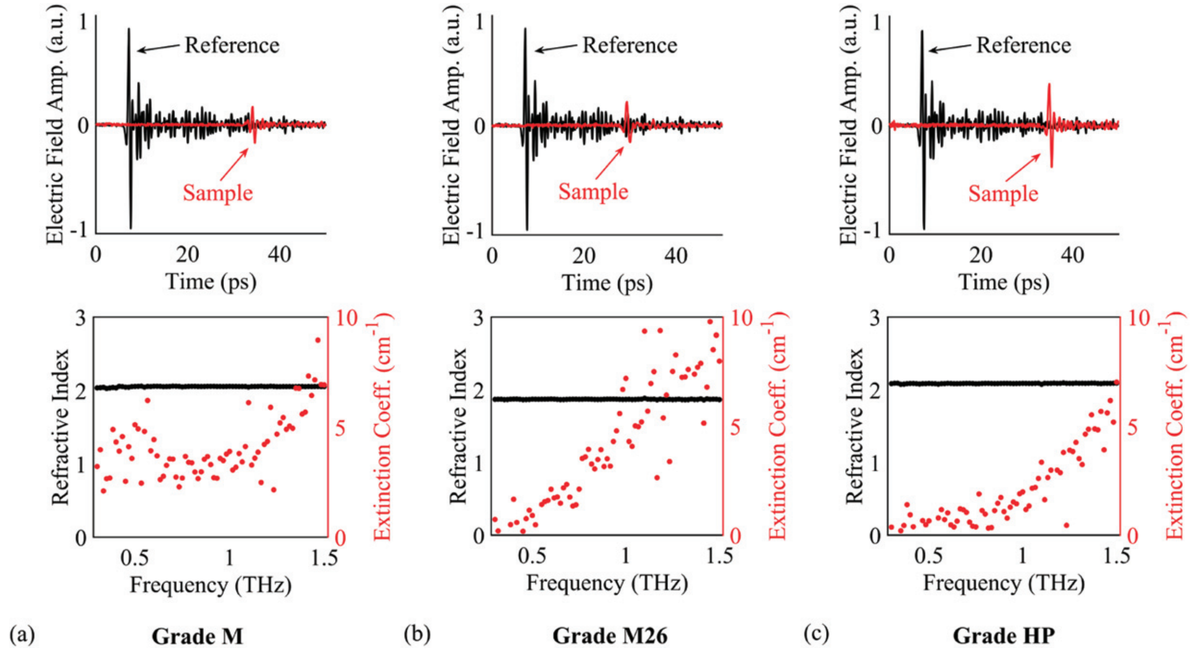

Figure 4. Representative THz pulses and extracted ordinary ray optical properties from measurements of 0.3 in-thick samples of grades (a) M, (b) M26, and (c) HP BN composite.

measurement results, and section 4.3 discusses the bounded plasma measurements.

4.1. Boundary properties

The ordinary ray optical properties of each boundary were independently measured to enable extraction of the complex plasma refractive index from the bounded plasma measurements. Figure 4 shows representative measured refractive index and extinction coefficients, as well as representative sample and reference THz pulse electric fields, measured in 0.3 in-thick samples of each BN grade. The refractive index and extinction coefficient are related to the complex refractive index by equation (11). The average refractive index is 2.06 for grade M, 1.87 for grade M26, and 2.09 for grade HP. The refractive index of each BN composite grade, within the measurement range, does not vary by more than 0.01 as a function of THz frequency. Applying the uncertainty quantification methodology of Withayachumnankul *et al* [38] yields a maximum uncertainty of less than 1% across all resolved THz frequencies.

The extinction coefficient, on average, increases exponentially with THz frequency for all three grades. Grades M26 and HP feature similarly low extinction coefficients on the order of 1 cm^{-1} at frequencies below 0.5 THz, but the extinction coefficient rises to approximately 4 cm^{-1} at 1 THz in grade M26 and only 2 cm^{-1} at 1 THz in grade HP. Grade M, on the other hand, does not have any measured extinction coefficients below 2 cm^{-1}. Consequently, as observed in the reference and sample pulses in figure 4, grade M induces the most THz pulse attenuation and grade HP induces the least THz pulse attenuation.

Variation of the reported extinction coefficient about the trends is caused by absorption resonances and scattering in the samples and by general measurement uncertainties. These effects are amplified by the relatively large sample thicknesses. Uncertainty is driven by the signal-to-noise ratio (SNR) of the real part of the THz spectrum and varies with THz frequency. Applying the uncertainty quantification methodology of Withayachumnankul *et al* [38] results in a minimum uncertainty of approximately 10% near 1 THz and maximum uncertainty of approximately 30% near the plot extrema and at water absorption lines.

It should additionally be noted that the extinction coefficient is commonly reported as a smoothed curve fit in the THz-TDS literature. We report unfiltered extinction coefficients in figure 4 because unfiltered results from each boundary, and not curve fits, were used in the computation of plasma properties from the bounded plasma measurements.

To our knowledge, the THz refractive indices and extinction coefficients of grades M, M26, and HP BN are not published elsewhere in the literature. However, curve fits of the THz properties of grade HBR BN, manufactured by Momentive Performance Materials, were measured and published by Naftaly *et al* [24]. HBR BN is of similar composition to HP BN (hcp BN hot-pressed in a calcium borate binder) and therefore serves as a useful benchmark material. Figure 5 compares these HBR curve fits to the raw HP data shown in figure 4(c). Even though the compared materials are not identical, the raw HP data closely match the previously published HBR curve fits.

4.2. Plasma measurements

Figure 6 shows sample and reference THz pulses recorded with the ICP discharge operating at an input power of 100 W and measured pressure of 1 Torr. In each case the plasma was bounded by two 0.3 in-thick walls, according to the

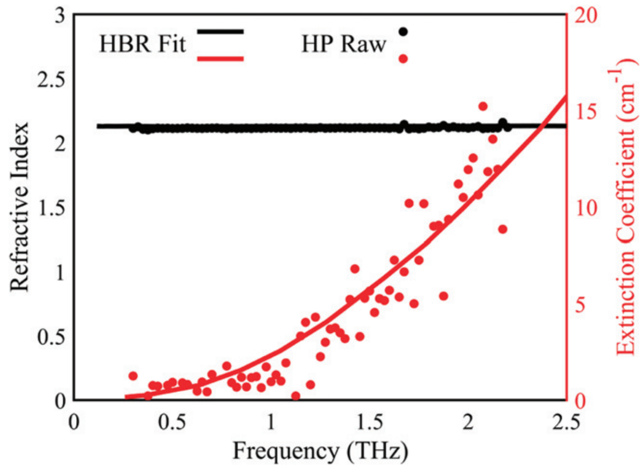

Figure 5. Comparison of grade HP BN THz properties to previously published curve fits of grade HBR BN THz properties. HBR BN data from [24].

configuration shown in figure 2(b). The pulse SNR is significantly reduced for the grade M and M26 cases, but the signals are still clearly discernable above the noise.

Figure 7 shows the measured average electron density and collision frequency for the 0.3 in-thick boundary cases for a measured pressure of 1 Torr. The unbounded case is also included in the figure for comparison. The error bar width encompasses a 90% Bayesian credibility interval [28]. In some cases, the electron collision frequency was below the detectable limit of the THz-TDS system; these cases feature Bayesian posterior probability density functions that match the input priors and are therefore not plotted. The severe reduction in SNR caused by the M BN boundaries precludes determination of the electron collision frequency for all operating conditions.

For input powers ranging from 20 to 60 W, the electron density of the plasma bounded by M BN approximately follows that of the unbounded configuration. However, starting at 80 W, though the electron density of the M BN continues to approximately follow a linearly increasing trend with power, the values diverge and become smaller than the unbounded densities. The electron density results with M26 and HP BN boundaries deviate substantially from the unbounded case. The M26 BN boundaries appear to cause the electron density to alternately increase and decrease with discharge power, though many of these variations are within the error of the measurement. The HP BN boundaries cause the electron density to peak at a discharge power of 100 to 120 W and then decrease with discharge power from 140 to 200 W. For most discharge powers, the plasma bounded by M BN has a larger electron density than that bounded by HP BN, which, in turn, has a larger electron density than the plasma bounded by M26 BN.

The uncertainty of the electron collision frequency measurements is highly dependent upon the SNR of the signal magnitude. Due to the severe loss of SNR caused by propagation of the THz pulses through the plasma boundaries, the uncertainty of these measurements is high and electron collision frequency trends are consequently difficult to establish. However, figure 7(b) does indicate that, for a given discharge power, the electron collision frequency is typically lower with boundaries than without boundaries. Another notable observation is that many of the reported electron collision frequency values are larger (sometimes by an order of magnitude) than those predicted by first-order consideration of argon electron–neutral momentum transfer cross sections [39].

In order to provide further understanding of the observed trends, additional measurements were taken with two additional M26 BN boundary configurations: one with 0.3 in-thick boundaries and discharge pressure of 5 Torr and one with 0.1 in-thick boundaries and discharge pressure of 1 Torr. Figure 8 shows the resulting electron densities and collision frequencies for these configurations. The unbounded and M26 BN results from figure 7 are also plotted for comparison. The electron densities of the two additional M26 BN cases follow the same approximate trend as that of the HP BN case; the electron density rises, peaks, and then falls with increasing discharge power. The loss of SNR caused by propagation of the THz pulses through the plasma boundaries precludes precise discernment of the electron collision frequency trends, but it is evident that the collision frequency of the plasma with 0.1 in-thick boundaries approximately matches that of the unbounded plasma until it begins to decrease with increasing discharge power between 140 W and 160 W.

4.3. Discussion of plasma measurement results

4.3.1. Electron density. The unbounded plasma electron density results display a simple linear trend that is similar in shape and magnitude to other THz-TDS and Langmuir probe studies of similar discharges [18, 20]. However, the electron densities measured in the various bounded plasma configurations show markedly different behavior. There are two possible reasons for this result: either the boundaries alter the discharge plasma physics or the boundaries interfere with the THz-TDS measurement.

As discussed in section 1, previous measurements have shown that shielding the plasma from the THz radiation with BN-SiO_2 does not inherently alter the measurement [19]. However, plasma properties in shielded measurements are, as in unshielded measurements, extracted with the well-established unbounded plasma relationship given by equation (2). By contrast, the bounded plasma properties are extracted via equation (9). Because this relationship requires input from measured boundary properties, the impact of plasma boundaries on the electron density measurement requires further discussion.

A common approximation made in unbounded THz-TDS plasma diagnostics is to simplify equation (2) so that the electron density can be extracted directly from the phase of the ratio of the sample and reference electric field spectra, without input of the magnitude [18, 20–23, 31, 32]. This approximation is derived assuming that $\nu \ll \omega_p$ and $\omega_p^2 \ll \omega^2$, and these two conditions are met in the data presented here. The electron density, therefore, is almost exclusively a function of the phase of the spectral ratio. Additionally, due to the relatively small values of the boundary absorption coefficients required

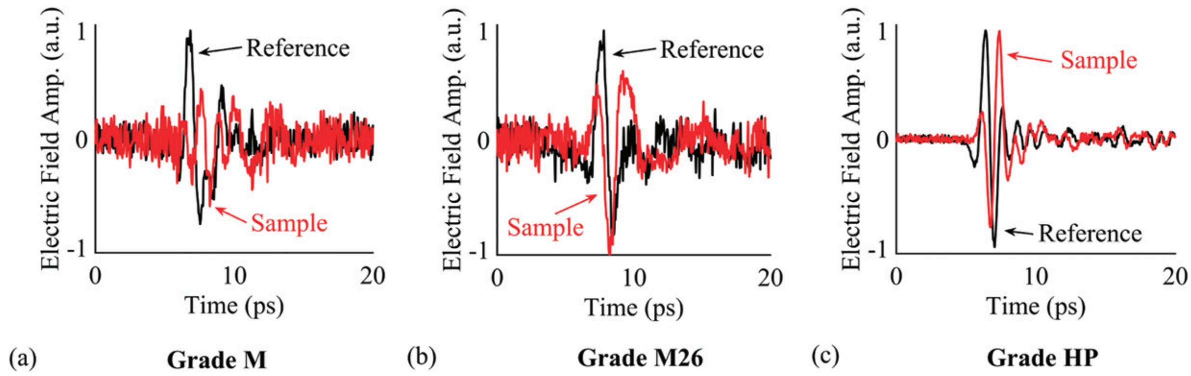

Figure 6. Sample and reference THz pulses recorded with the RF ICP discharge operating at 1 Torr, 100 W. The plasma was bounded by two 0.3 in-thick grade (a) M, (b) M26, and (c) HP BN composite walls.

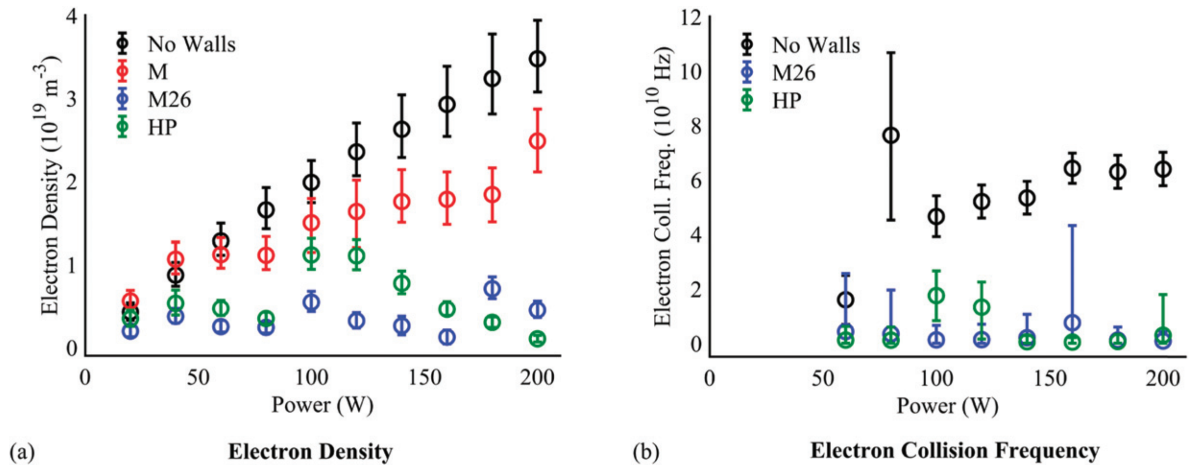

Figure 7. Measurement results for (a) electron density and (b) electron collision frequency with the plasma bounded by two 0.3 in-thick walls. The error bars encompass a 90% credibility interval.

to permit propagation of detectable THz pulses through the boundaries, the imaginary portion of each complex boundary transmission coefficient typically has negligible impact on the phase of the spectral ratio. Consequently, the impact of the transmission coefficients on the phase of the spectral ratio is commonly ignored in analysis of standard THz-TDS measurements of solid-state samples [38]. Taken together, these two common approximations imply that, for the plasma conditions studied here, inclusion of the boundaries in equation (9) should have little impact on the computed electron density.

To test the impact of the boundaries on the equations, we compared the plasma property results produced by equations (2) and (9) at a single THz frequency for a particular measurement result. In order to remove the influence of the Bayesian framework and measurement artifacts, we made the comparison with assumed hypothetical plasma parameters equal to the electron density and collision frequency measured with the M26 BN-bounded plasma operating at 1 Torr and 100 W. We input these values, along with the measured M26 BN optical properties, into equation (9) to determine the output spectral ratio at 1 THz. We then input this spectral ratio into equation (2) and inverted the relation to extract the electron density and collision frequency. The resulting output electron density differed by less than 0.0002% from the input, but the output electron collision frequency differed by 74%.

This result supports the conclusion that the boundaries strongly impact the electron collision frequency computation but have virtually no effect on the electron density computation. The large differences between the electron densities measured with and without boundaries are, therefore, not explained by any boundary-induced uncertainties in equation (9); in fact, for our plasma conditions, the electron density of the bounded plasma can be extracted with equation (2) with negligible reduction in accuracy.

Because the presence of boundary material in the THz pulse path has been previously shown to not impact the THz-TDS measurement [19] and because the boundary properties have negligible impact on the electron density measurement, we conclude that our electron density results are indicative of changes in the discharge physics caused by the boundaries. Though a full accounting and simulation of the boundary-induced changes to the electron density are outside the scope of this work, we can provide possible causes for the trends we

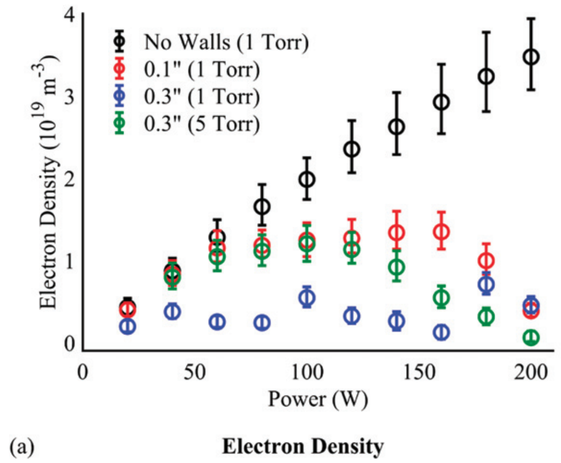

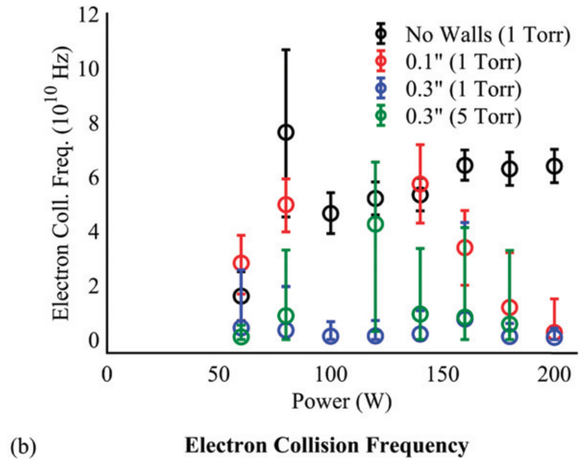

Figure 8. Measurement results for (a) electron density and (b) electron collision frequency with the plasma bounded by two grade M26 BN composite walls. The error bars encompass a 90% credibility interval.

observed. We also invite future modeling efforts to investigate these causes in more detail.

The large differences in peak electron density between the bounded cases may possibly be explained by differences in porosity between the BN composite grades. Due to the configuration of the ICP discharge, input argon must pass through the boundaries before it is ionized. The neutral pressure inside the bounded region is therefore less than the reported neutral pressure measured outside the bounded region. Previous work has shown that the porosity of grades M, M26, and HP BN composite can vary by more than 100% on a lot-to-lot basis [40]. Based on the results found here, it is likely that the grade M BN composite boundaries featured the largest porosity. This resulted in significantly larger neutral gas density in the region between the M BN boundaries than within the M26 and HP BN boundaries, thereby enabling the production of a higher-density plasma.

Some evidence for this explanation is given by figure 8(a), which shows the measured electron density for the various M26 BN boundary cases. The 0.3 in- and 0.1 in-thick M26 BN samples were machined from the same stock and should therefore have approximately the same porosity coefficients. The 0.1 in-thick boundaries have higher total porosity and therefore allow more argon into the bounded region, thereby resulting in a larger electron density for the same reported pressure. Increasing the reported discharge pressure to 5 Torr with the 0.3 in-thick boundaries produces a similar effect; the larger overall discharge pressure results in a higher neutral pressure within the bounded region and thereby results in a higher-density plasma.

Other factors, such as secondary electron emission, may help explain the electron density trends observed in the plasma bounded by M26 and HP BN. As more energy is input into the plasma by the antenna, the electrons become more energized and begin to strike the boundary walls with sufficient energy to produce secondary electrons with lower energy. The replacement of high-energy electrons with low-energy electrons at the boundaries becomes more pronounced at higher discharge powers and may lead to reduced ionization rate [41].

The boundaries can also interfere with the coupling of power into the plasma by acting as barriers through which the induced electric and magnetic fields must propagate. This effect has been shown to substantially influence plasma properties and may also contribute to the observed trends [42, 43].

4.3.2. Electron collision frequency. The large electron collision frequency uncertainties in figures 7(b) and 8(b) are caused by the severe loss of SNR from the transmission of THz pulses through the boundaries. In general, meaningful trends cannot be extracted from the bounded plasma electron collision frequency results. However, as noted in section 4.2, some of the electron collision frequencies are up to an order of magnitude larger than that predicted by first-order consideration of argon electron–neutral momentum transfer cross sections [39].

A possible explanation for this discrepancy is artificial attenuation of the THz beam by plasma refraction and plasma-interface reflections. However, refraction is accounted for in the Bayesian data analysis technique [28] and reflections are accounted for by inclusion of the boundary transmission coefficients in equation (9). Reflections may be ignored in the unbounded case because, due to the small (real) refractive index mismatch between the plasma and vacuum, artificial attenuation caused by plasma-vacuum reflections changes the ratio of the sample and reference electric field spectra to a degree that is well below that detectable by the THz-TDS system [16, 28].

An alternate explanation is that the measured electron collision frequencies are simply larger than what is predicted by first-order consideration of electron–neutral momentum cross sections [44]. This work is not the first to report unexpectedly large electron collision frequencies; the phenomenon has been experimentally observed in a variety of plasma discharges [7, 8, 16, 45–48] and has been reproduced in high-fidelity computational discharge models [44]. This work does, however, provide some of the most direct experimental evidence of the discrepancy.

5. Conclusion

In this paper, we experimentally demonstrated the capability of THz-TDS to noninvasively probe plasmas bounded and optically shielded by Hall thruster wall material. Though we found the reduction in the SNR caused by propagation of the THz pulses through the wall material sometimes precluded determination of the electron collision frequency, measurement of the electron density was not impacted. The plasma boundaries were observed to cause the electron density trends to deviate substantially from that of the unbounded plasma, but supplementary results demonstrated that these changes were indicative of changes in plasma physics rather than boundary-induced measurement errors. Our results are not directly applicable to Hall thruster discharge physics, but they do highlight the necessity for bounded plasma diagnostics.

We conclude that THz-TDS is presently a candidate to perform noninvasive electron density measurements of the plasma inside the Hall thruster discharge channel. Future advances in THz emission and detection technology may sufficiently improve the SNR to enable THz-TDS to provide robust electron collision frequency measurements as well.

Acknowledgments

Nathan Brown was supported by the National Science Foundation Graduate Research Fellowship under Grant No. DGE-1650044, an Achievement Reward for College Scientists sponsored by Siemens, and a Georgia Tech Institute for Materials Graduate Student Fellowship sponsored by BASF. Sandia National Laboratories is a multimission laboratory managed and operated by National Technology & Engineering Solutions of Sandia, LLC, a wholly owned subsidiary of Honeywell International Inc., for the United States Department of Energy's National Nuclear Security Administration under Contract DE-NA0003525. This paper describes objective technical results and analysis. Any subjective views or opinions that might be expressed in the paper do not necessarily represent the views of the United States Department of Energy or the United States Government.

Data availability statement

The data that support the findings of this study are available upon reasonable request from the authors.

ORCID iDs

Nathan P Brown https://orcid.org/0000-0003-3654-2357
Adam M Steinberg https://orcid.org/0000-0001-6571-6673

References

[1] Zhurin V V, Kaufman H R and Robinson R S 1999 *Plasma Sources Sci. Technol.* **8** R1–R20
[2] Goebel D M and Katz I 2008 *Fundamentals of Electric Propulsion: Ion and Hall Thrusters* (New York: Wiley)
[3] Charles C 2009 *J. Phys. D: Appl. Phys.* **42** 163001
[4] Mazouffre S 2016 *Plasma Sources Sci. Technol.* **25** 033002
[5] Lev D, Myers R M, Lemmer K M, Kolbeck J, Koizumi H and Polzin K 2019 *Acta Astronaut.* **159** 213–27
[6] Brown N P and Walker M L R 2020 *Appl. Sci.* **10** 3775
[7] Meezan N B, Hargus W A and Cappelli M A 2001 *Phys. Rev.* E **63** 026410
[8] Jorns B 2018 *Plasma Sources Sci. Technol.* **27** 104007
[9] Schinder A M, Rimoli J J and Walker M L R 2016 *J. Propul. Power* **33** 433–47
[10] Staack D, Raitses Y and Fisch N J 2004 *Appl. Phys. Lett.* **84** 3028–30
[11] Linnell J A and Gallimore A D 2006 *Phys. Plasmas* **13** 093502
[12] Ellison C L, Raitses Y and Fisch N J 2012 *Phys. Plasmas* **19** 013503
[13] Chiu Y-h, Austin B L, Williams S, Dressler R A and Karabadzhak G F 2006 *J. Appl. Phys.* **99** 113304
[14] Hargus W A and Cappelli M A 2001 *Appl. Phys.* B **72** 961–9
[15] Washeleski R L, Meyer E J and King L B 2013 *Rev. Sci. Instrum.* **84** 105101
[16] Jamison S P, Shen J, Jones D R, Issac R C, Ersfeld B, Clark D and Jaroszynski D A 2003 *J. Appl. Phys.* **93** 4334–6
[17] Kolner B H, Conklin P M, Buckles R A, Fontaine N K and Scott R P 2005 *Appl. Phys. Lett.* **87** 151501
[18] Ando A, Kurose T, Reymond V, Kitano K, Kitahara H, Takano K, Tani M, Hangyo M and Hamaguchi S 2011 *J. Appl. Phys.* **110** 073303
[19] Brown N P, Steinberg A M, Deibel J A and Walker M L 2020 *AIAA Propulsion and Energy Forum* pp 2020–3647
[20] Jang D, Uhm H S, Jang D, Hur M S and Suk H 2016 *Plasma Sources Sci. Technol.* **25** 065008
[21] Meier S M, Tsankov T V, Luggenhölscher D and Czarnetzki U 2017 *J. Phys. D: Appl. Phys.* **50** 245202
[22] Meier S M, Hecimovic A, Tsankov T V, Luggenhölscher D and Czarnetzki U 2018 *Plasma Sources Sci. Technol.* **27** 035006
[23] Kang K, Lee S, Jang D, Kim J and Suk H 2020 *Plasma Phys. Control. Fusion* **62** 125008
[24] Naftaly M and Leist J 2013 *Appl. Opt.* **52** B20–B5
[25] Duvillaret L, Garet F and Coutaz J-L 1996 *IEEE J. Sel. Top. Quantum Electron.* **2** 739–46
[26] Withayachumnankul W, Ferguson B, Rainsford T, Mickan S and Abbott D 2006 *Fluct. Noise Lett.* **06** L227–39
[27] Kolner B H, Buckles R A, Conklin P M and Scott R P 2008 *IEEE J. Sel. Top. Quantum Electron.* **14** 505–12
[28] Brown N P, Grauer S J, Deibel J A, Walker M L R and Steinberg A M 2021 *Opt. Express* **29** 4887–901
[29] Withayachumnankul W and Naftaly M 2014 *J. Infrared Milli Terahz Waves* **35** 610–37
[30] Neu J and Schmuttenmaer C A 2018 *J. Appl. Phys.* **124** 231101
[31] Brown N P 2020 *Development and Evaluation of Terahertz Time-Domain Spectroscopy for Electric Propulsion Plasma Diagnostics* (Atlanta, USA: Georgia Institute of Technology)
[32] Heald M A and Wharton C B 1965 *Plasma Diagnostics with Microwaves* (New York: Wiley)
[33] Stix T H 1992 *Waves in Plasmas* (New York: American Institute of Physics)
[34] Auston D H, Cheung K P and Smith P R 1984 *Appl. Phys. Lett.* **45** 284–6
[35] Wu Q and Zhang X C 1995 *Appl. Phys. Lett.* **67** 3523–5
[36] Planken P C M, Nienhuys H-K, Bakker H J and Wenckebach T 2001 *J. Opt. Soc. Am.* B **18** 313–7
[37] Lee Y-S 2009 *Principles of Terahertz Science and Technology* (New York: Springer)
[38] Withayachumnankul W, Fischer B M, Lin H and Abbott D 2008 *J. Opt. Soc. Am.* B **25** 1059–72

[39] Pitchford L C *et al* 2013 *J. Phys. D: Appl. Phys.* **46** 334001
[40] Mackey J, Salem J, Stanford M, Kamhawi H, McEnerney B and Hofer R 2020 *44th Int. Conf. and Expo on Advanced Ceramics and Composites*
[41] Gascon N, Dudeck M and Barral S 2003 *Phys. Plasmas* **10** 4123–36
[42] Stittsworth J A and Wendt A E 1996 *Plasma Sources Sci. Technol.* **5** 429–35
[43] Wu Y and Lieberman M A 2000 *Plasma Sources Sci. Technol.* **9** 210–8
[44] Lafleur T, Chabert P, Turner M M and Booth J P 2013 *Phys. Plasmas* **20** 124503
[45] Godyak V A, Piejak R B, Alexandrovich B M and Kolobov V I 1998 *Phys. Rev. Lett.* **80** 3264–7
[46] Lee C A, Chen G, Arefiev A V, Bengtson R D and Breizman B N 2011 *Phys. Plasmas* **18** 013501
[47] Lundin D, Helmersson U, Kirkpatrick S, Rohde S and Brenning N 2008 *Plasma Sources Sci. Technol.* **17** 025007
[48] Mikellides I G, Katz I, Goebel D M and Jameson K K 2007 *J. Appl. Phys.* **101** 063301